

Cite this: *Chem. Sci.*, 2021, 12, 9176

All publication charges for this article have been paid for by the Royal Society of Chemistry

# Large breathing effect induced by water sorption in a remarkably stable nonporous cyanide-bridged coordination polymer†

Michał Magott,<sup>ID</sup> <sup>\*a</sup> Bartłomiej Gawęł,<sup>ID</sup> <sup>b</sup> Marcin Sarewicz,<sup>ID</sup> <sup>c</sup>  
Mateusz Reczyński,<sup>ID</sup> <sup>a</sup> Karolina Ogorzały,<sup>ID</sup> <sup>a</sup> Wacław Makowski<sup>ID</sup> <sup>a</sup>  
and Dawid Pinkowicz<sup>ID</sup> <sup>\*a</sup>

While metal–organic frameworks (MOFs) are at the forefront of cutting-edge porous materials, extraordinary sorption properties can also be observed in Prussian Blue Analogs (PBAs) and related materials comprising extremely short bridging ligands. Herein, we present a bimetallic nonporous cyanide-bridged coordination polymer (CP)  $\{[\text{Mn}(\text{imH})]_2[\text{Mo}(\text{CN})_6]\}_n$  (**1Mn**; imH = imidazole) that can efficiently and reversibly capture and release water molecules over tens of cycles without any fatigue despite being based on one of the shortest bridging ligands known – the cyanide. The sorption performance of  $\{[\text{Mn}(\text{imH})]_2[\text{Mo}(\text{CN})_6]\}_n$  matches or even outperforms MOFs that are typically selected for water harvesting applications with perfect sorption reversibility and very low desorption temperatures. Water sorption in **1Mn** is possible due to the breathing effect (accompanied by a dramatic cyanide-framework transformation) occurring in three well-defined steps between four different crystal phases studied structurally by X-ray diffraction structural analysis. Moreover, the capture of  $\text{H}_2\text{O}$  by **1Mn** switches the EPR signal intensity of the  $\text{Mn}^{\text{II}}$  centres, which has been demonstrated by *in situ* EPR measurements and enables monitoring of the hydration level of **1Mn** by EPR. The sorption of water in **1Mn** controls also its photomagnetic behavior at the cryogenic regime, thanks to the presence of the  $[\text{Mo}^{\text{IV}}(\text{CN})_6]^{4-}$  photomagnetic chromophore in the structure. These observations demonstrate the extraordinary sorption potential of cyanide-bridged CPs and the possibility to merge it with the unique physical properties of this class of compounds arising from their bimetallic character (e.g. photomagnetism and long-range magnetic ordering).

Received 13th April 2021

Accepted 1st June 2021

DOI: 10.1039/d1sc02060a

rsc.li/chemical-science

## Introduction

Metal–organic frameworks (MOFs) dominated the field of porous molecule-based materials due to their outstanding sorption characteristics<sup>1,2</sup> including the capture of small molecules (e.g.  $\text{H}_2$ ,  $\text{CO}_2$ ,  $\text{CH}_4$ ),<sup>3–7</sup> water,<sup>8,9</sup> alcohols<sup>10–13</sup> or compounds as large as aromatics<sup>14,15</sup> or proteins.<sup>16,17</sup> Some of the recent advancements in this field cover exceptional water harvesting applications<sup>18–22</sup> and the construction of adsorption-driven heat

pumps.<sup>23–25</sup> Therefore, it is widely believed that MOFs outperform other water sorption materials, as they can indeed absorb moisture at much lower vapor pressures than active carbons and may be regenerated at significantly lower temperatures than silica gels or zeolites. Nonetheless, MOFs are currently being challenged by covalent organic frameworks (COFs),<sup>26–29</sup> which in principle are more stable against  $\text{H}_2\text{O}$ , as opposed to the hydrolysis susceptible metal-carboxylate moieties present in MOFs.<sup>30</sup>

In this whirlwind of MOF/COF possibilities, CN-bridged coordination polymers (CN-CPs) – Prussian Blue Analogues (PBAs) and related cyanide-bridged frameworks – remain underrated or even omitted as potential sorbents despite some promising reports of  $\text{H}_2$  (ref. 31–34) and ammonia<sup>35–37</sup> sorption. This is caused by another common belief that these materials show low fatigue resistance limited to several sorption cycles and can release toxic components in the process – like the first examples of MOFs before the seminal work by Yaghi *et al.*<sup>38</sup> and before the demonstration of reversible bond breaking in the water-stable DMOF-TM showing state-of-the-art water sorption capabilities.<sup>39</sup> Overcoming this stereotype is crucial for further

<sup>a</sup>Faculty of Chemistry, Jagiellonian University, Gronostajowa 2, 30-387 Kraków, Poland. E-mail: [michal.magott@uj.edu.pl](mailto:michal.magott@uj.edu.pl); [dawid.pinkowicz@uj.edu.pl](mailto:dawid.pinkowicz@uj.edu.pl)

<sup>b</sup>Department of Materials Science and Engineering, Norwegian University of Science and Technology (NTNU), 7491 Trondheim, Norway

<sup>c</sup>Department of Molecular Biophysics, Faculty of Biochemistry, Biophysics and Biotechnology, Jagiellonian University, Gronostajowa 7, 30-387 Kraków, Poland

† Electronic supplementary information (ESI) available: Additional structural diagrams, TGA profiles, PXRD patterns, water adsorption isotherms, DSC curves, EPR, IR and UV-vis spectra, magnetic and photomagnetic data and CIF files. CCDC [2046137, 2046138, 2048781, 2048780 and 2048779]. For ESI and crystallographic data in CIF or other electronic format see DOI: 10.1039/d1sc02060a

progress in the field of multifunctional molecular materials as CN-CPs offer the possibility of fine tuning of many different functionalities including magnetism or magnetic and photo-magnetic switching upon solvent removal/exchange.<sup>40–47</sup> This in turn will potentially lead to ground-breaking magnetic sponge systems<sup>48,49</sup> operational at room temperature.

In this work, we address this issue by presenting state-of-the-art water sorption properties and exceptional cyclability of a completely nonporous cyanide-bridged framework  $\{[\text{Mn}^{\text{II}}(\text{imH})]_2[\text{Mo}^{\text{IV}}(\text{CN})_8]\}_n$  (**1Mn**) (the anhydrous form of  $\{[\text{Mn}^{\text{II}}(\text{imH})(\text{H}_2\text{O})_2]_2[\text{Mo}^{\text{IV}}(\text{CN})_8] \cdot 4\text{H}_2\text{O}\}_n$  (**1Mn·8H<sub>2</sub>O**), reported by Shen *et al.* in 2006)<sup>50</sup> and the analogue of the low-temperature magnetic sponge-like system  $\{[\text{Mn}^{\text{II}}(\text{imH})]_2[\text{Nb}^{\text{IV}}(\text{CN})_8]\}_n$  (ref. 45) as well as the photomagnetic sponge  $\{[\text{Mn}^{\text{II}}(\text{imH})]_2[\text{W}^{\text{IV}}(\text{CN})_8]\}_n$ .<sup>47</sup> Despite the obvious lack of porosity demonstrated in the nitrogen sorption experiment, **1Mn** shows three water-induced quasi-phase transitions, accompanied by a very large breathing effect<sup>51–53</sup> and a substantial change in the cyanide bridging pattern fully understood based on the powder X-ray diffraction structural analysis. The three-step breathing process is fully reversible and exceptionally fatigue resistant over tens of adsorption/desorption cycles, with the complete preservation of crystallinity and very high water uptake exceeding 25% w/w.

Apart from the exceptional water sorption and cyclability, **1Mn** exhibits marked magnetic and photomagnetic changes upon water capture. Similar effects were previously reported in paramagnetic MOFs where strong interdependence between sorption and other physical properties occurs.<sup>54–60</sup> In some cases, the profound structural and electronic changes induced by guest molecules enable the characterization/monitoring of the sorption process using EPR spectroscopy. This can be done directly in the case of paramagnetic guests<sup>61–65</sup> or indirectly by analysing the *g*-factor shift of paramagnetic metal centers as in some Cu<sup>II</sup>-based porous materials.<sup>54,66–68</sup> Noteworthy, EPR spectroscopy is commonly applied to study the state of the paramagnetic active sites doped into the mesoporous hosts such as zeolites in various catalytic processes.<sup>69–72</sup> In the case of **1Mn**, presented herein, the state of the Mn<sup>II</sup> sites was successfully monitored in the real time by employing *in situ* EPR spectroscopy during the

adsorption/desorption of water molecules. Structural and electronic changes within the coordination sphere of Mn<sup>II</sup> affect also the low-temperature photo-induced magnetization of the compound which is evidenced by detailed photo-magnetic studies.

## Results and discussion

### Structure, breathing behaviour and sorption properties

$\{[\text{Mn}^{\text{II}}(\text{imH})(\text{H}_2\text{O})_2]_2[\text{Mo}^{\text{IV}}(\text{CN})_8] \cdot 4\text{H}_2\text{O}\}_n$  (**1Mn·8H<sub>2</sub>O**) was prepared according to the modified literature procedure<sup>50</sup> by combining water solutions of manganese(II) chloride and imidazole with potassium octacyanomolybdate(IV), affording yellow crystals suitable for single crystal X-ray diffraction (SCXRD; see Experimental section for details). **1Mn·8H<sub>2</sub>O** forms a three-dimensional coordination framework in *C2/c* space group, with two octahedral manganese(II) cations coordinated by one imidazole ligand (disordered between two positions), three nitrogen atoms of the  $[\text{Mo}^{\text{IV}}(\text{CN})_8]^{4-}$  in a *mer* configuration and two *aqua* ligand in *cis* disposition (Table 1 and Fig. S1†). Each octacyanomolybdate(IV) connects six manganese(II) centres and the Mn<sub>2</sub>Mo unit is accompanied by four crystallization water molecules located in the channels along the crystallographic *c* direction (Fig. 1c). The 3-D framework of **1Mn·8H<sub>2</sub>O** can be described as a “crossed-ladder” cyanide bridging pattern, similar to that depicted in Fig. 2a and S2 in the ESI,† with two sets of coordination ladders cross-linking at the Mo<sup>IV</sup> centres.

The coordination and crystallization water molecules can be removed completely by heating **1Mn·8H<sub>2</sub>O** above 60 °C in a dry nitrogen atmosphere, and the coordination skeleton of the resulting  $\{[\text{Mn}^{\text{II}}(\text{imH})]_2[\text{Mo}^{\text{IV}}(\text{CN})_8]\}_n$  (**1Mn**) (Fig. 1f and 2c) remains stable up to 250 °C (TGA, Fig. S3†). Interestingly, water adsorption/desorption isotherm recorded at 298 K shows that the solvent loss is in fact a three-step process (Fig. 1a), proceeding through two intermediate phases. In the desorption branch, the **1Mn·8H<sub>2</sub>O** phase is stable down to *ca.* 20% of the relative humidity (RH). The first intermediate mass plateau is observed in the 10–14% RH range corresponding to  $\Delta m/m_0$  of 9.3–10.6% (Fig. 1a, II;  $\Delta m/m_0$  denotes mass change relative to the anhydrous state,  $m_0$ ). This step is in good agreement with

**Table 1** Summary of the main structural features of **1Mn·8H<sub>2</sub>O**, **1Mn·3H<sub>2</sub>O**, **1Mn·2H<sub>2</sub>O** and **1Mn** formed during the reversible dehydration/hydration cycles

Abbreviation	Chemical formula	Structure determination method	Space group	Coordination geometry of the Mn <sup>II</sup> ions	Coordination numbers of the Mn <sup>II</sup> ions	Number of CN-bridges per Mo <sup>IV</sup>
<b>1Mn·8H<sub>2</sub>O</b>	$\{[\text{Mn}^{\text{II}}(\text{imH})(\text{H}_2\text{O})_2]_2[\text{Mo}^{\text{IV}}(\text{CN})_8] \cdot 4\text{H}_2\text{O}\}_n$	SCXRD	<i>C2/c</i>	Octahedron/octahedron	6/6	6
<b>1Mn·3H<sub>2</sub>O</b>	$\{[\text{Mn}^{\text{II}}(\text{imH})(\text{H}_2\text{O})_2][\text{Mn}^{\text{II}}(\text{imH})(\text{H}_2\text{O})][\text{Mo}^{\text{IV}}(\text{CN})_8]\}_n$	PXRD	<i>P1̄</i>	Distorted octahedron/trigonal bipyramid	6/5	6
<b>1Mn·2H<sub>2</sub>O</b>	$\{[\text{Mn}^{\text{II}}(\text{imH})(\text{H}_2\text{O})]_2[\text{Mo}^{\text{IV}}(\text{CN})_8]\}_n$	PXRD	<i>C2/c</i>	Trigonal bipyramid/trigonal bipyramid	5/5	6
<b>1Mn</b>	$\{[\text{Mn}^{\text{II}}(\text{imH})]_2[\text{Mo}^{\text{IV}}(\text{CN})_8]\}_n$	PXRD	<i>P1̄</i>	Distorted tetrahedron/trigonal bipyramid	4/5	7



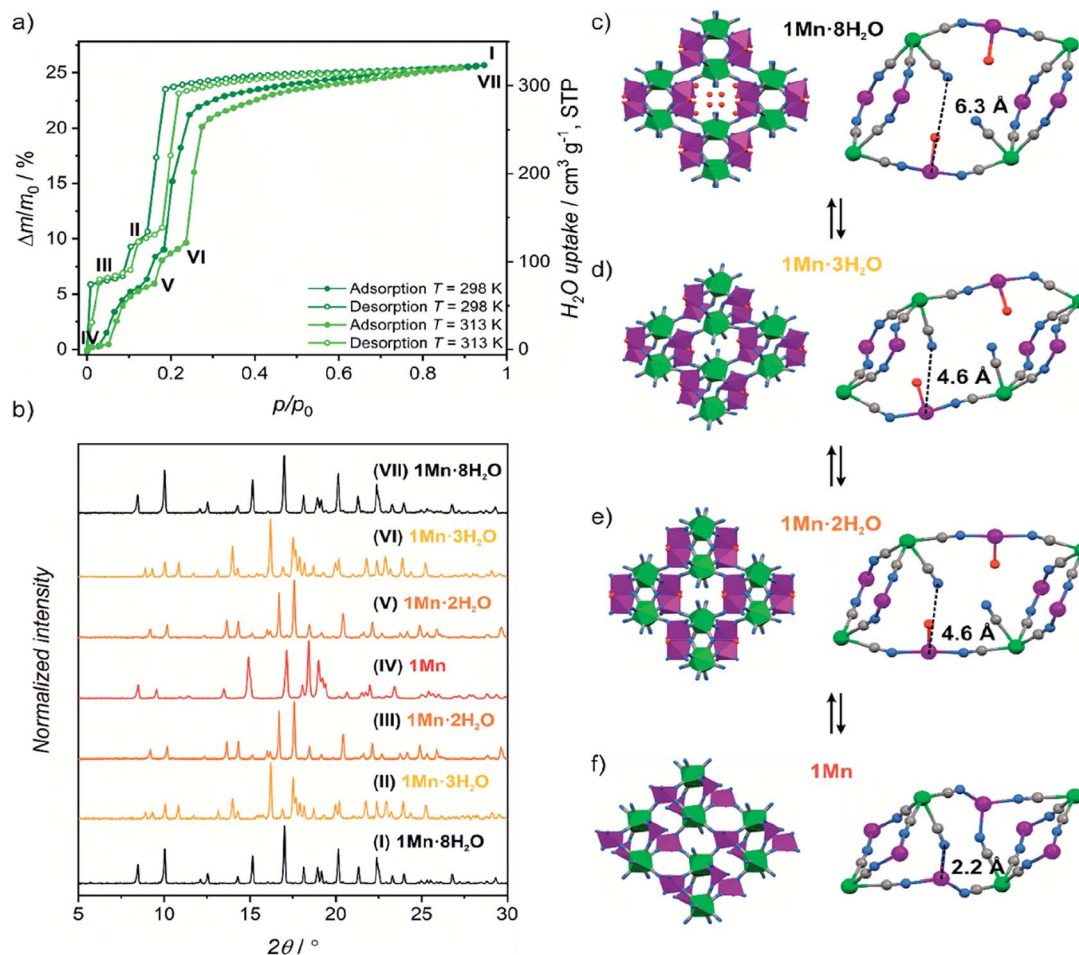


Fig. 1 (a) Water sorption/desorption isotherms for  $1\text{Mn} \cdot 8\text{H}_2\text{O}$  at 298 K and 313 K. Roman numerals enumerate different dehydration/hydration stages. (b) PXRD patterns observed for phases denoted in Fig. 1a. (c–f) Schematic representation of structural changes occurring during  $1\text{Mn} \cdot 8\text{H}_2\text{O}$  transformation between different crystalline phases. Imidazole molecules and hydrogen atoms were omitted for clarity.

$\{\text{Mn}^{\text{II}}(\text{imH})(\text{H}_2\text{O})_2\}[\text{Mn}^{\text{II}}(\text{imH})(\text{H}_2\text{O})][\text{Mo}^{\text{IV}}(\text{CN})_8]_n$  composition (calculated  $\Delta m/m_0 = 9.8\%$  corresponds to 3 water molecules), which would account for simultaneous removal of four crystallization water molecules and one coordinated water molecule. Indeed, powder X-ray diffraction (PXRD) confirms the appearance of a new crystalline phase  $1\text{Mn} \cdot 3\text{H}_2\text{O}$  obtained under conditions corresponding to point II in Fig. 1a (Fig. 1b, (II)).

Upon further decrease in relative humidity down to 1–8% RH range, another mass plateau emerges for  $\Delta m/m_0 = 6.1\text{--}6.6\%$  (Fig. 1a, (III)), which is close to 6.5% predicted for  $\{\text{Mn}^{\text{II}}(\text{imH})(\text{H}_2\text{O})_2\}[\text{Mo}^{\text{IV}}(\text{CN})_8]_n$  ( $1\text{Mn} \cdot 2\text{H}_2\text{O}$ ). The PXRD experiment shows complete disappearance of  $1\text{Mn} \cdot 3\text{H}_2\text{O}$  reflections at this step and the emergence of a new powder pattern for  $1\text{Mn} \cdot 2\text{H}_2\text{O}$  is depicted in Fig. 1b, (III). Passing dry nitrogen over the sample produces anhydrous  $1\text{Mn}$ , accompanied by the final changes in the PXRD pattern (Fig. 1b, (IV)). The rehydration process shows distinct hysteresis in water sorption isotherm, yet powder X-ray diffraction confirms that it proceeds through the same crystalline phases as during dehydration (Fig. 1a and b: (V, VI and VII)). Overall, the stepwise water adsorption isotherm for  $1\text{Mn}$  at 298 K shows the water uptake of

$0.26 \text{ g}_{\text{water}} \text{ g}^{-1}$  at  $p/p_0 = 0.9$ , but already reaches  $0.225 \text{ g g}^{-1}$  at  $p/p_0 = 0.3$ .

Upon solvent removal crystals of  $1\text{Mn} \cdot 8\text{H}_2\text{O}$  crack, precluding the determination of the crystal structures of the dehydrated phases by means of SCXRD. Therefore structures of compounds  $1\text{Mn} \cdot 3\text{H}_2\text{O}$ ,  $1\text{Mn} \cdot 2\text{H}_2\text{O}$  and  $1\text{Mn}$  were modelled by Rietveld refinement of the respective PXRD patterns (Fig. S4–S6†). The most significant structural features of the three dehydrated phases are summarized in Table 1.

In the first step of dehydration, the water-filled channels of  $\{\text{Mn}^{\text{II}}(\text{imH})(\text{H}_2\text{O})_2\}[\text{Mo}^{\text{IV}}(\text{CN})_8] \cdot 4\text{H}_2\text{O}\}_n$   $1\text{Mn} \cdot 8\text{H}_2\text{O}$  are emptied and one coordinated water molecule per formula unit is removed (Fig. 1c and d), which leads to a 14.0% shrinkage of the unit cell. Thus, the initially symmetry equivalent manganese(II) centres are diversified into the distorted octahedral  $[\text{Mn}^{\text{II}}(\text{imH})(\text{H}_2\text{O})_2(\mu\text{-NC})_3]$  and trigonal bipyramidal  $[\text{Mn}^{\text{II}}(\text{imH})(\text{H}_2\text{O})(\mu\text{-NC})_3]$  moieties in the resulting  $\{\text{Mn}^{\text{II}}(\text{imH})(\text{H}_2\text{O})_2\}[\text{Mn}^{\text{II}}(\text{imH})(\text{H}_2\text{O})][\text{Mo}^{\text{IV}}(\text{CN})_8]_n$   $1\text{Mn} \cdot 3\text{H}_2\text{O}$  framework (see Table 1) with a similar “crossed-ladder” bridging pattern as that of the parent  $1\text{Mn} \cdot 8\text{H}_2\text{O}$ . This decreases the lattice symmetry down to  $P\bar{1}$  space group. The



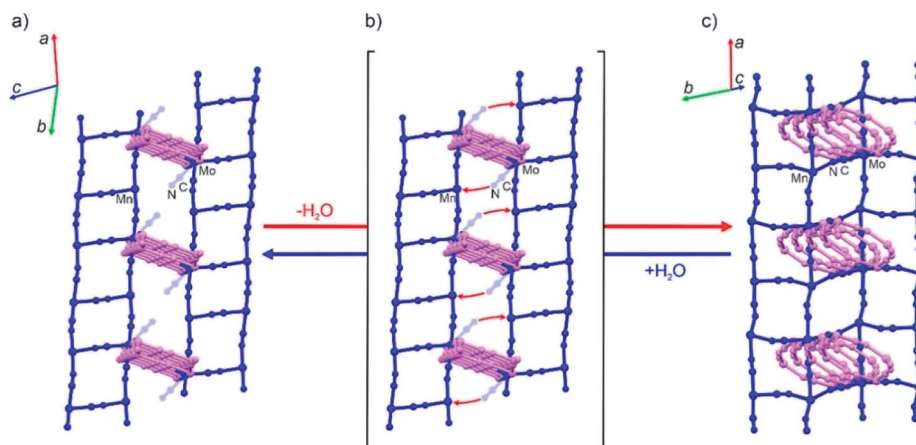


**Fig. 2** Simplified structural diagrams showing the change of the cyanide bridging pattern in the last step of the dehydration of **1Mn**·2H<sub>2</sub>O (a) accompanied by the additional CN-bridge formation (b) which finally yields anhydrous **1Mn** (c). The initial CN-bridged skeleton of **1Mn**·2H<sub>2</sub>O comprises two sets of color-coded (pink and blue) "ladder" motifs intersecting at the Mo<sup>IV</sup> nodes with six bridging CN<sup>−</sup> ligands (three per each "ladder") (a). Upon desolvation only the blue "ladders" transform into "square grids" due to the additional CN-bridge formation (b) while the pink "ladders" adapt their geometry in the final CN-bridged scaffold of **1Mn** (c). The Mo<sup>IV</sup> nodes in the anhydrous **1Mn** utilize seven CN<sup>−</sup> ligands for bridging towards Mn<sup>II</sup> ions (three per pink "ladder" and four per "blue square grid"). Please see Fig. S2 in the ESI† for the same figure with color-coded atoms.

removal of an additional coordinated water molecule restores the *C*<sub>2</sub>/*c* symmetry, by converting the remaining six-coordinated manganese(II) into a trigonal bipyramidal motif in the {[Mn<sup>II</sup>(imH)(H<sub>2</sub>O)]<sub>2</sub>[Mo<sup>IV</sup>(CN)<sub>8</sub>]}<sub>n</sub> **1Mn**·2H<sub>2</sub>O framework (Fig. 1e and 2a). In this step, only a minimal change of the unit cell volume is observed (−1.6%).

The most pronounced transformation is observed in the last dehydration step. Removal of the remaining two *aqua* ligands enables the formation of an additional cyanide bridge in {[Mn<sup>II</sup>(imH)]<sub>2</sub>[Mo<sup>IV</sup>(CN)<sub>8</sub>]}<sub>n</sub> **1Mn**, enforcing further 11.7% decrease in the unit cell volume as well as the dramatic cyanide bridging pattern change depicted in Fig. 2. The "crossed-ladder" pattern changes into a "ladders-crossing-square-grids" coordination scaffold. In the final structure (triclinic, *P* $\bar{1}$ , Fig. 1f) the tetracoordinate [Mn<sup>II</sup>(imH)(μ-NC)<sub>3</sub>] adopts distorted vacant trigonal bipyramidal geometry and the pentacoordinate [Mn<sup>II</sup>(imH)(μ-NC)<sub>4</sub>] centre becomes a distorted trigonal bipyramid. Each octacyanomolybdate(IV) unit forms seven cyanide bridges to the neighbouring manganese(II) centres in the anhydrous form.

IR spectra recorded during the dehydration experiment reveal changes consistent with those described above – the bands associated with H<sub>2</sub>O molecules disappear and the bands in the cyanide stretching vibration region change significantly for each phase (please see Fig. S7–S9 as well as the detailed description of the IR spectra in the ESI†).

The aforementioned dehydration-driven stepwise transformations are mirrored in the rehydration experiments, as depicted in Fig. 1a and b. This includes also the bridging pattern changes from "ladders-crossing-square-grids" to "crossed ladders" (Fig. 2). The unit cell volume per formula unit changes from 996 Å<sup>3</sup> in **1Mn** to 1332 Å<sup>3</sup> in **1Mn**·8H<sub>2</sub>O, which accounts for the 34% total change between the anhydrous and the fully hydrated phases, respectively. Such tremendous unit

cell expansion is unprecedented among other porous cyanide-bridged polymers<sup>46,84–92</sup> and falls within the range observed for flexible MOFs (Table 2). Interestingly, the structure of the anhydrous **1Mn** does not show any solvent accessible voids and hence – no permanent porosity. This is evidenced by type II nitrogen adsorption isotherm recorded at 77 K (Fig. 3). The observed N<sub>2</sub> uptake of 16 cm<sup>3</sup> g<sup>−1</sup> at *p*/*p*<sub>0</sub> = 1.0 is an order of magnitude smaller than observed for MOFs showing similar total water uptake (such as DMOF-TM<sup>39,93</sup> or MOF-801 (ref. 9 and 74)) and even smaller than reported for the typically nonporous materials such as Zr<sub>6</sub>O<sub>4</sub>(OH)<sub>4</sub>(SQU)<sub>5.25</sub>(CH<sub>3</sub>COO)<sub>1.5</sub> MOF based on a squaric acid.<sup>94</sup> Therefore combined structural and sorption studies of **1Mn** show that initial chemisorption of four water molecules opens the channels in its structure, which only then enables physisorption of the remaining water. Although similar water-induced gate-opening behaviour was previously reported for JUK-8,<sup>80</sup> SIFSIX-23-Cu<sup>83</sup> and the MIL-53 family,<sup>51,95,96</sup> to the best of our knowledge **1Mn** constitutes the first case among non-reticular materials.

**1Mn**·8H<sub>2</sub>O shows marvellous stability during dehydration–rehydration cycling taking into account the accompanying huge unit cell volume variations. This was confirmed by dynamic vapor sorption (DVS) experiments. The sample mass was monitored as the relative humidity was switched between 0 and 95% at 298 K in 57 cycles (Fig. 4a; see Fig. S10† for full representation of 57 adsorption–desorption cycles). The observed mass change of 26.7% between 0 and 95% RH agrees perfectly with the value of 26.2% expected for transition between **1Mn** and **1Mn**·8H<sub>2</sub>O. No change in the curve profile is observed in 57 cycles performed over the course of 430 hours. Powder X-ray diffraction pattern collected for the sample rehydrated after the end of the cycling experiment shows no difference from the one recorded for the pristine sample at the beginning of the experiment (Fig. 4b). Apart from the apparent broadening of the





Table 2 Selected examples of MOFs showing large water sorption or water-driven breathing behaviour<sup>a</sup>

Compound	Water uptake ( $p/p_0 = 0.3$ )/ $\text{cm}^3 \text{g}^{-1}$ , STP	Total water uptake $/\text{cm}^3 \text{g}^{-1}$ , STP	Water-induced breathing behaviour (total volume change: $\Delta V/V_{\text{anhydrous}}$ )	Ref.
CAU-10	275	365	No	9 and 73
MOF-801	380	450	No	9 and 74
UiO-66	125	535	No	9 and 75
MOF-841	550	640	No	9
Mg-MOF-74	605	750	No	9 and 76
$\text{Co}_2\text{Cl}_2\text{BTDD}$	1100	1200	No	77
$\text{Ni}_2\text{Cl}_2\text{BTDD}$	240	1350	No	20
Cr-MIL-101	150	1700	No	78 and 79
JUK-8	90	315	Yes (24.5%)	80
<b>1Mn</b>	<b>280</b>	<b>320</b>	<b>Yes (34%)</b>	<b>This work</b>
Cr-MIL-53	<i>n/a</i>	110 <sup>b</sup>	Yes (−47%)	51
Al-MIL-53	90	120	Yes (−49%)	81 and 82
SIFSIX-23-Cu	160	325	Yes (53%)	83
Fe-MIL-88	<i>n/a</i>	850 <sup>b</sup>	Yes (85%)	52

<sup>a</sup> Values in italic are lower than those reported for **1Mn**. <sup>b</sup> Total water uptake determined only from the amount of water in the crystal structure.

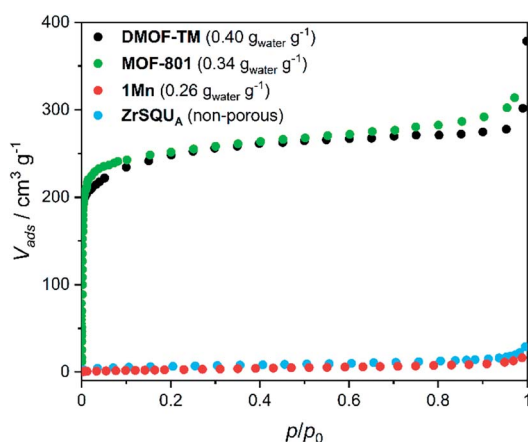


Fig. 3 Nitrogen adsorption isotherms at 77 K for **1Mn** and selected MOFs. Water loading values at  $p/p_0 = 0.9$  and  $T = 298$  K presented in the parentheses were reported in ref. 39 for DMOF-TM and ref. 9 for MOF-801. BET isotherms for MOFs were adapted from ref. 39, 74 and 93.

diffraction peaks (see Fig. S11†), the PXRD patterns of the fully hydrated samples before and after the cycling experiment do not show any significant differences. The peak broadening can be explained by the decrease in the grain size resulting from the repetitive breaking of the crystallites in the consecutive dehydration/rehydration cycles, as evidenced by SEM pictures collected for the sample before and after cycling experiments (Fig. S12†). Nonetheless, both DVS and PXRD experiments confirm the perfect stability of the material in water sorption experiments, with full retainment of its water uptake and crystallinity up to 58 cycles.

High water-stability and water uptake at low relative pressures are required for application in atmospheric water harvesting.<sup>9,97</sup> For this purpose materials with low desorption temperatures are preferable, in order to easily retrieve a liquid condensate from the hydrated sorbent. By comparing the

adsorption isotherms at 25 °C and 40 °C (Fig. S13†), we conclude that the material should produce around 0.172  $\text{g}_{\text{water}} \text{g}^{-1}$  under 0.95 kPa water pressure (30% RH at 25 °C) upon cycling between these two temperatures. Such a process should switch the material between the **1Mn**·8H<sub>2</sub>O and **1Mn**·2H<sub>2</sub>O hydration states with a simultaneous release of all crystallization water molecules and a half of the coordinated ones at only 40 °C. To confirm that **1Mn** can be used for moisture harvesting, we performed a cycling experiment which emulates desert conditions in the daytime (40 °C, 10% RH) and at night (25 °C, 30% RH; Fig. S14†).<sup>9</sup> The cycling process revealed a real working capacity of 0.164  $\text{g} \text{g}^{-1}$  which approaches the theoretical value deduced from the adsorption isotherms.

The observed release of the chemisorbed water at low temperatures is surprising, as chemisorption is usually associated with high adsorption enthalpy. Therefore we decided to estimate the average adsorption enthalpy of water in **1Mn** by employing the van't Hoff equation to the water adsorption isotherms, as well as integrating differential scanning calorimetry (DSC) curve obtained during the sample dehydration (Fig. S15 and 16,† see the Experimental section for details). Both methods give similar results, with effective adsorption enthalpy of 66  $\text{kJ mol}^{-1}$  per water molecule deduced from the van't Hoff equation and 64  $\text{kJ mol}^{-1}$  obtained from the DSC experiment (it is important to note that effective adsorption enthalpy includes energetic effects of water adsorption and cyanide bridge breaking that proceed simultaneously). The small discrepancy results from the difference in desorption temperatures (25–40 °C for the isotherm method, and >70 °C for the DSC experiment). The obtained adsorption enthalpy (64–66  $\text{kJ mol}^{-1}$ ) is much higher than that reported for hydrophilic MOFs<sup>23</sup> and in line with the chemisorption of half of the water molecules. Nonetheless, the strong binding of water does not prevent its easy removal at low temperatures, as demonstrated in the previous parts of the manuscript. This must be associated with fast desorption kinetics, which can be quantified assuming first



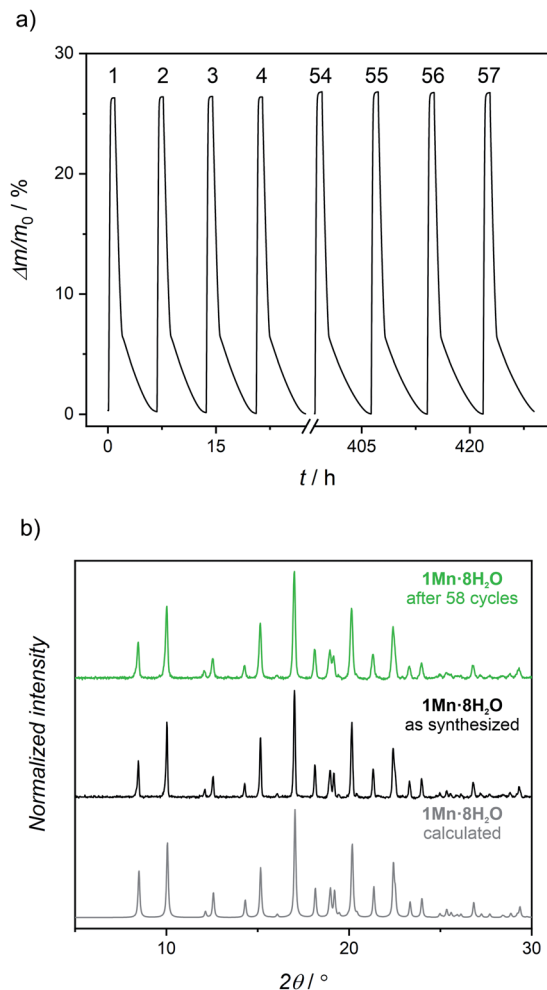


Fig. 4 (a) Water cycling stability test (0% RH dehydration – 95% RH rehydration) of **1Mn·8H<sub>2</sub>O** at 298 K (numbers above the curve enumerate the consecutive dehydration–rehydration cycles; Fig. S10† shows all 57 cycles). (b) Powder X-ray diffraction patterns for **1Mn·8H<sub>2</sub>O**: calculated from the single-crystal structure (grey), experimental for pristine sample (black) and experimental after 58 dehydration–rehydration cycles at 25 °C (green).

order kinetics of dehydration and applying the Kissinger equation<sup>98,99</sup> to the TGA results at different heating rates (Fig. S17–19†):

$$\ln \frac{\beta}{T_m^2} = \text{const} - \frac{E_a}{RT_m}$$

where  $\beta$  – heating rate,  $T_m$  – the temperature at the maximum rate of mass change ( $dm/dT$ ), and  $E_a$  – activation energy. This method yields apparent activation energy of 101(7) kJ mol<sup>−1</sup> in the first dehydration step, which in the TGA experiment accounts for **1Mn·8H<sub>2</sub>O** → **1Mn·2H<sub>2</sub>O** transformation and 65(3) kJ mol<sup>−1</sup> in the second dehydration step, which ends in the production of anhydrous **1Mn**. While the first value is within the 91–111 kJ mol<sup>−1</sup> range reported for functionalized MIL-101,<sup>23</sup> the second value is unexpectedly small and approaching water adsorption enthalpy for **1Mn** at low water loadings. We hypothesize that this may result from the cyanide

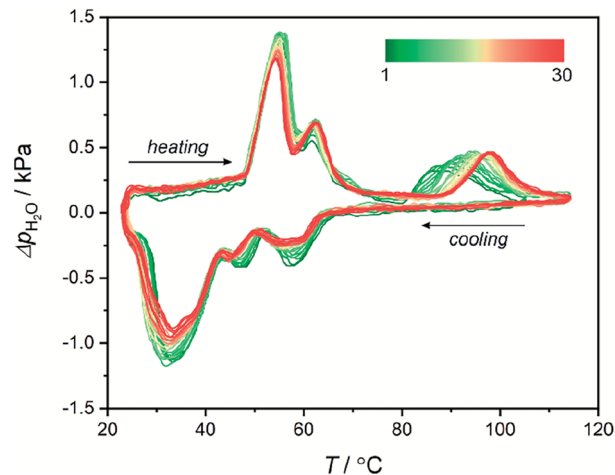


Fig. 5 30 heating/cooling QE-TPDA profiles obtained for **1Mn·8H<sub>2</sub>O** at a temperature sweep rate of 0.75 °C min<sup>−1</sup> using H<sub>2</sub>O (2.4 kPa)/He mixture as a carrier gas.

bridge formation in the **1Mn·2H<sub>2</sub>O** → **1Mn** step (Fig. 2), which affects the dehydration process.

Water sorption in **1Mn** was also tested by quasi-equilibrated temperature programmed desorption and adsorption (QE-TPDA).<sup>100–102</sup> In this method, the sorption of volatile compounds is studied by cyclic heating and cooling of a quartz tube containing the sample, under the flow of adsorbate (in this case – water vapor) dispersed in a stream of helium gas. The QE-TPDA profiles present positive signals when excess water is desorbed from the sample or negative signals when carrier gas is being depleted of the adsorbate. Recently, the method has been proven useful in studies of water sorption in MOFs<sup>103,104</sup> and cyanide-bridged assemblies.<sup>105</sup> The QE-TPDA profiles of **1Mn·8H<sub>2</sub>O** demonstrate a three-step desorption process (Fig. 5), which is in line with the aforementioned water desorption isotherm. While the first two steps remain almost unchanged in the 30 consecutive sorption/desorption cycles, the high-temperature one, corresponding to the **1Mn·2H<sub>2</sub>O** → **1Mn** transformation, drifts to higher temperatures from 86 °C in the first cycle to 98 °C in cycles 20<sup>th</sup>–30<sup>th</sup>. It is worth noting that these temperatures are higher than in the TGA experiments because in QE-TPDA the water vapor pressure at 20 °C is 100% RH (TGA analysis is performed using dry nitrogen).

The shift in the final desorption temperature is hard to explain, as no visible decrease in water loading can be deduced from the QE-TPDA signal after 30 cycles of temperature driven desorption. Powder X-ray diffractogram obtained after the experiment (30 adsorption/desorption cycles in the 23–115 °C range) shows that the compound preserves crystallinity, but shows small unidentified reflections indicating some thermal fatigue/damage (Fig. S20†). Possibly, it may indicate minor structural changes, such as the appearance of defects in the structure affecting the last desorption step. Still, the QE-TPDA analysis confirms the exceptionally good stability of **1Mn** during 23–115 °C thermal cycling in a humid environment.

## EPR spectroscopy

Paramagnetic manganese(II) nodes in the structure of **1Mn** enable water sorption studies using electron paramagnetic resonance (EPR) spectroscopy. Manganese(II) cations usually show a negligible contribution from the orbital momentum, sustaining sufficiently long spin relaxation times to observe the EPR spectrum at room temperature. This is accompanied by relatively small zero field splitting (ZFS) effect (in the range of the X-band microwave frequency), which is influenced by the local coordination environment of the metal ions. Therefore EPR may be utilized to track changes in manganese(II) geometry upon solvation/desolvation at room temperature and in real time. In our experiment, powdered **1Mn**·8H<sub>2</sub>O was subjected to a continuous flow of nitrogen (either dry or saturated with water vapours) inside the EPR resonator (for details please refer to Experimental section). **1Mn**·8H<sub>2</sub>O shows a broad signal at  $g = 2.00$  demonstrated in Fig. 6a (scans 0–10) and Fig. S21,† which originates from the overlap of transitions between different  $m_s$  states for  $S = 5/2$ .

Drying the sample leads to the rapid drop in the signal intensity and its broadening (Fig. 6a). The lowest EPR signal

intensity at 320.6 mT is reached around scan no. 25 (Fig. 6b and S22†). The hydration stage at this step can be identified by comparison with the EPR spectra recorded for the isolated phases (Fig. S21 and S23†). It was assigned as a mixture of **1Mn**·2H<sub>2</sub>O and **1Mn**·3H<sub>2</sub>O, in line with the DVS measurement, in which the observed mass change in the intermediate step of dry gas dehydration can be attributed to **1Mn**·2H<sub>2</sub>O (Fig. 4a). Upon further drying, the intensity of the transition increases slightly for over 50 scans (Fig. 6b), which corresponds to a slow formation of the anhydrous **1Mn**. Saturating purge gas with water vapours leads to a very fast signal recovery with no observation of the intermediate steps depicted in Fig. 6, exactly as in the DVS experiment.

In order to study phase-dependent variation of ZFS in **1Mn**·8H<sub>2</sub>O, we prepared its isomorphous cadmium analogue  $\{[\text{Cd}(\text{imH})(\text{H}_2\text{O})_2]_2[\text{Mo}^{\text{IV}}(\text{CN})_8] \cdot 4\text{H}_2\text{O}\}_n$  (**2Cd**·8H<sub>2</sub>O) (Fig. S24†). Resolution of six transitions resulting from hyperfine splitting caused by manganese  $I = 5/2$  nucleus was achieved for the diamagnetic matrix of **2Cd**·8H<sub>2</sub>O doped with manganese(II) (**2Cd**·8H<sub>2</sub>O:Mn), but left ZFS unresolved (Fig. S25†). This suggests only minimal zero-field splitting, which was estimated using EasySpin software<sup>106</sup> to be no larger than  $|D| = 0.04 \text{ cm}^{-1}$ . Unlike **1Mn**·8H<sub>2</sub>O, dehydration of **2Cd**·8H<sub>2</sub>O leads to its amorphization and decomposition, which is observed in the TGA measurement at the temperature *ca.* 80 °C lower than for the Mn-analogue (Fig. S3†). Nevertheless, the crystallinity of the dry amorphous solid dried under vacuum at room temperature can be restored by rehydration at 100% RH (Fig. S26†). Despite the restoration of the crystallinity, the water sorption capacity of **2Cd** decreases significantly in the subsequent QE-TPDA sweeps (Fig. S27†), indicating irreversible damage of the coordination skeleton.

Amorphization is even more pronounced for **2Cd**·8H<sub>2</sub>O:Mn, which after dehydration shows no diffraction peaks in the PXRD experiment (Fig. S28†). Thus, we were unable to determine the exact parameters of ZFS for **1Mn**, **1Mn**·2H<sub>2</sub>O and **1Mn**·3H<sub>2</sub>O by studying the Mn-doped Cd-analogues as the corresponding crystalline phases could not be identified. This highlights the key role of manganese(II) for the stabilization and “breathing” performance of the CN-bridged framework upon water adsorption/desorption. Apparently, manganese(II) not only provides paramagnetic properties of the material but is responsible for the structural integrity of the framework.

## Magnetic and photomagnetic properties

Results of the EPR spectroscopy are fully supported by magnetometry of **1Mn** and its hydrated states, as depicted in Fig. S29 and 30.† Room-temperature  $\chi T$  products for all four compounds are within 8.8–9.0 cm<sup>3</sup> K mol<sup>−1</sup> range, as expected for two independent manganese(II) cations characterized by  $g = 2.0$ . The  $\chi T(T)$  curves show a distinct decrease at the lowest temperatures, which is more pronounced for more dehydrated phases, as quantified by fitting the experimental points to the Curie–Weiss law (Fig. S29,† inset) that yields the following Weiss constants: −0.7 K for **1Mn**·8H<sub>2</sub>O, −1.2 K for **1Mn**·3H<sub>2</sub>O, −1.5 K for **1Mn**·2H<sub>2</sub>O and −3.6 K for **1Mn**. It can be ascribed to increasing ZFS and/or stronger antiferromagnetic interactions,

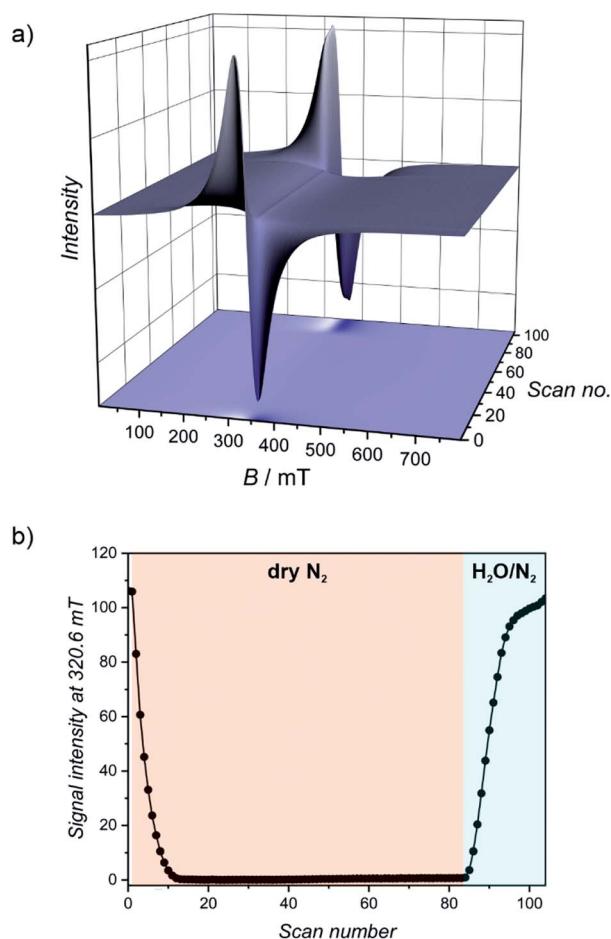


Fig. 6 (a) Continuous wave X-band (9.7 GHz) EPR spectra obtained for **1Mn**·8H<sub>2</sub>O during dehydration (scans 0–84) and rehydration (scans 85–105) at room temperature. (b) EPR signal intensity for **1Mn**·8H<sub>2</sub>O upon dry N<sub>2</sub> purging (scan numbers 0–84) and rehydration in N<sub>2</sub> saturated with water vapor (scan numbers 85–105).



due to the decreasing distances between Mn(II) centres associated with dehydration and unit cell volume contraction. The influence of stronger antiferromagnetic interactions explains also the shape of the  $M(H)$  dependencies, showing a deviation from the Brillouin function expected for two non-interacting Mn<sup>II</sup> centers which becomes more distinct with the dehydration level in the  $1\text{Mn} \cdot 8\text{H}_2\text{O} \rightarrow 1\text{Mn} \cdot 3\text{H}_2\text{O} \rightarrow 1\text{Mn} \cdot 2\text{H}_2\text{O} \rightarrow 1\text{Mn}$  series (Fig. S30†). Nonetheless, all phases behave as paramagnets in the 2–300 K range, as expected for manganese(II) cations separated by the diamagnetic octacyanomolybdate(IV) groups.

The octacyanomolybdate(IV) anion was previously demonstrated to behave as an intrinsic photomagnetic chromophore in several bimetallic CN-bridged systems.<sup>107–109</sup> Therefore we decided to study the photomagnetic properties of **1Mn** and **1Mn**·8H<sub>2</sub>O at low temperatures. Both compounds strongly respond to 450 nm light (irradiation wavelength selected based on the UV-vis spectra; Fig. S31†) with a 13-fold increase of the magnetization in the case of **1Mn** and a 16-fold increase for **1Mn**·8H<sub>2</sub>O at 10 K (Fig. S32†). After irradiation, **1Mn** shows clear bifurcation of ZFC-FC curves at  $T_c = 72$  K (Fig. 7), which is slightly lower than for its octacyanotungstate(IV) analogue with  $T_c = 93$  K.<sup>47</sup> This behaviour is assumed to originate from the photo-induced formation of  $S = 1$  Mo<sup>IV</sup> (ref. 109) which couples magnetically with  $S = 5/2$  Mn<sup>II</sup> centres and enables ferrimagnetic ordering of the network.<sup>108</sup> More importantly, photo-induced magnetic ordering at  $T_c = 40$  K is also demonstrated by the **1Mn**·8H<sub>2</sub>O in contrast to the lack of the photomagnetic response in the case of its [W<sup>IV</sup>(CN)<sub>8</sub>]-based analogue  $\{[\text{Mn}^{\text{II}}(\text{imH})(\text{H}_2\text{O})_2]_2[\text{W}^{\text{IV}}(\text{CN})_8] \cdot 4\text{H}_2\text{O}\}_n$ .<sup>47</sup> However, the photomagnetic behaviour of both compounds **1Mn** and **1Mn**·8H<sub>2</sub>O shows signs of irradiation damage. The latter preserves the characteristics of long-range magnetic ordering even after 2 hours of thermal relaxation at 240 K (Fig. S33–36†). As far as we know, **1Mn** and  $\{[\text{Mn}^{\text{II}}(\text{imH})]_2[\text{W}^{\text{IV}}(\text{CN})_8]\}_n$  constitute the first

examples of isostructural octacyanometalate(IV)-based photomagnets in which both Mo<sup>IV</sup> and W<sup>IV</sup> congeners demonstrate photo-induced magnetic ordering.<sup>41</sup> This enables comparison of their photomagnetic functionalities, with the former responding to light even in the fully hydrated state and the latter demonstrating significantly higher magnetic ordering temperature and better reversibility of the photomagnetic effect.

## Conclusions

A completely nonporous cyanide-bridged coordination polymer  $\{[\text{Mn}(\text{imH})]_2[\text{Mo}(\text{CN})_8]\}_n$  with exceptional water sorption, stability, and cyclability is demonstrated.  $\{[\text{Mn}(\text{imH})]_2[\text{Mo}(\text{CN})_8]\}_n$  shows outstanding breathing effect with a 34% volume increase as a result of >25% w/w water uptake. The breathing of the framework is accompanied/caused by a reversible breaking/formation of an additional Mn–N coordination bond between Mn<sup>II</sup> centres and CN<sup>−</sup> ligands. This behaviour occurs in three well-defined steps and is completely reversible over tens of water vapor pressure- or temperature-swing cycles with full retention of the water sorption capacity and the crystallinity of the compound. It clearly shows that cyanide-bridged coordination polymers demonstrate competitive sorption properties, and the alleged instability of their CN-bridged coordination skeleton is merely a common belief. Simultaneous changes in the cyanide bridging pattern as well as the metal centre geometry in the presented systems significantly affect both their magnetic and photomagnetic properties. They can be also tracked in real time using EPR spectroscopy.

The presented results demonstrate that cyanide-bridged coordination polymers and PBA analogues can combine exceptional sorption properties with various magnetic functionalities like photo-induced magnetization changes or long-range magnetic ordering affected by guest molecules. They constitute, therefore, a new competitive class of multifunctional sorption materials. This study re-establishes CN-CPs and PBAs as high-performance sorption materials with the potential to challenge current state-of-the-art MOFs.

## Experimental section

### Synthesis details

All reagents were used as supplied from commercial sources (Alfa Aesar). Potassium octacyanomolybdate(IV) was obtained according to the previously reported procedure.<sup>110</sup>

$\{[\text{Mn}^{\text{II}}(\text{imH})(\text{H}_2\text{O})_2]_2[\text{Mo}^{\text{IV}}(\text{CN})_8] \cdot 4\text{H}_2\text{O}\}_n$  (**1Mn**·8H<sub>2</sub>O). In order to prevent co-precipitation of MnO<sub>2</sub>, the synthesis was performed in an oxygen-free glovebox with the use of water deoxygenated by 12 h reflux under argon atmosphere. A solution containing 0.5 mmol (100 mg) of MnCl<sub>2</sub>·4H<sub>2</sub>O and 1.0 mmol (68 mg) of imidazole in 10 mL of water was mixed with a water solution of 0.1 mmol (50 mg) of potassium octacyanomolybdate(IV) dihydrate in 10 mL of water. After 48 h yellow column crystals were collected by decantation and dried in air (typical yield: ca. 30 mg, 40%). The purity was confirmed by elemental analysis and PXRD. Anal. calcd for C<sub>14</sub>H<sub>24</sub>Mn<sub>2</sub>N<sub>12</sub>O<sub>8</sub>Mo: C 24.20, H 3.48, N 24.22; found: C 24.43, H 3.16, N 24.29.

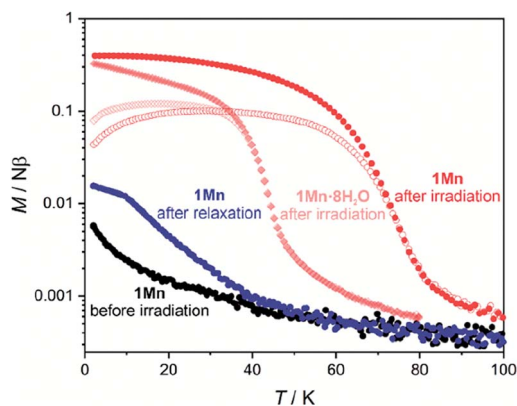


Fig. 7 Field-cooled (closed symbols) and zero field-cooled (open symbols) curves for **1Mn** (circles) and **1Mn**·8H<sub>2</sub>O (rhombi) under  $H_{\text{DC}} = 0.02$  T. Both samples were irradiated with  $\lambda = 450$  nm and  $P = 3\text{--}5$  mW light, thermal relaxation for **1Mn** was performed by heating to 315 K and stabilizing at this temperature for 1 hour. Complete magnetic/photomagnetic data for both **1Mn**·8H<sub>2</sub>O and **1Mn** are presented in Fig. S33 and S34 in the ESI.†





$[\text{Mn}^{\text{II}}(\text{imH})(\text{H}_2\text{O})_2][\text{Mn}^{\text{II}}(\text{imH})(\text{H}_2\text{O})][\text{Mo}^{\text{IV}}(\text{CN})_8]_n$  (**1Mn**·3H<sub>2</sub>O). Hand-milled crystals of **1Mn**·8H<sub>2</sub>O were kept for 12 hours in the desiccator above saturated water solution of lithium chloride at 298 K (RH = 11.3 ± 0.3%).<sup>111</sup>

$[\text{Mn}^{\text{II}}(\text{imH})(\text{H}_2\text{O})_2][\text{Mo}^{\text{IV}}(\text{CN})_8]_n$  (**1Mn**·2H<sub>2</sub>O). Hand-milled crystals of **1Mn**·8H<sub>2</sub>O were kept for 12 hours in the desiccator above saturated water solution of potassium hydroxide at 313 K (RH = 6.3 ± 0.4%).<sup>111</sup>

$[\text{Mn}^{\text{II}}(\text{imH})]_2[\text{Mo}^{\text{IV}}(\text{CN})_8]_n$  (**1Mn**). **1Mn**·8H<sub>2</sub>O was vacuum-dried ( $p \approx 10^{-2}$  mbar) over P<sub>4</sub>O<sub>10</sub> for 12 hours at room temperature

$[\text{Cd}^{\text{II}}(\text{imH})(\text{H}_2\text{O})_2]_2[\text{Mo}^{\text{IV}}(\text{CN})_8] \cdot 4\text{H}_2\text{O}$  (**2Cd**·8H<sub>2</sub>O). A solution containing 0.5 mmol (114 mg) of CdCl<sub>2</sub>·2.5H<sub>2</sub>O and 1.0 mmol (68 mg) of imidazole in 80 mL of water was mixed with the water solution of 0.1 mmol (50 mg) of potassium octacyanomolybdate(IV) dihydrate in 10 mL of water. After 24 h yellow needle crystals were collected by decantation and dried in air (typical yield: ca. 20 mg, 25%). The purity was confirmed by PXRD. Anal. calcd for C<sub>14</sub>H<sub>24</sub>Cd<sub>2</sub>N<sub>12</sub>O<sub>8</sub>Mo: C 20.76, H 2.99, N 20.78; found: C 22.45, H 2.56, N 21.71. The discrepancy between the calculated and observed composition results from solvent loss and concomitant decomposition of the compound after removing crystals from the mother liquor.

$[\text{Mn}_x\text{Cd}_{1-x}(\text{imH})(\text{H}_2\text{O})_2]_2[\text{Mo}^{\text{IV}}(\text{CN})_8] \cdot 4\text{H}_2\text{O}$  (**2Cd**·8H<sub>2</sub>O·**Mn**). In order to prevent co-precipitation of MnO<sub>2</sub>, synthesis was performed in an oxygen-free glovebox with the use of water deoxygenated by 12 h reflux under argon atmosphere. A solution containing 0.3 mmol (68 mg) of CdCl<sub>2</sub>·2.5H<sub>2</sub>O, 0.15 mmol (30 mg) of MnCl<sub>2</sub>·4H<sub>2</sub>O and 1.0 mmol (68 mg) of imidazole in 80 mL of water was mixed with a water solution of 0.1 mmol (50 mg) of potassium octacyanomolybdate(IV) dihydrate in 10 mL of water. After 24 h yellow needle crystals were collected by decantation and dried in air (typical yield: ca. 20 mg, 25%). The purity was confirmed by PXRD. Anal. calcd for C<sub>14</sub>H<sub>24</sub>Cd<sub>2</sub>N<sub>12</sub>O<sub>8</sub>Mo: C 20.76, H 2.99, N 20.78; found: C 23.22, H 2.50, N 22.12. The discrepancy between the calculated and observed composition results from solvent loss and concomitant decomposition of the compound after removing crystals from the mother liquor.

**2Cd** and **2Cd**·**Mn** were obtained from **2Cd**·8H<sub>2</sub>O and **2Cd**·8H<sub>2</sub>O·**Mn** respectively, which were vacuum-dried ( $p \approx 10^{-2}$  mbar) over P<sub>4</sub>O<sub>10</sub> for 12 hours at room temperature.

### Single crystal X-ray diffraction

SCXRD experiments were performed for **1Mn**·8H<sub>2</sub>O and **2Cd**·8H<sub>2</sub>O using Bruker D8 Quest Eco Photon50 CMOS diffractometer (Mo K $\alpha$  radiation, Triumph® monochromator). Single crystals were moved directly from mother liquor into cryo-oil to avoid solvent loss on air. Absorption corrections, data reduction and unit cell refinements were performed using SADABS and SAINT programs included in the Apex3 suite. The structures were solved using direct methods and refined anisotropically using weighted full-matrix least-squares on  $F^2$ .<sup>112–114</sup> Hydrogen atoms of the ligands were placed in calculated positions and refined as riding on the parent atoms. Structural diagrams were prepared using Mercury CSD 4.0.<sup>115</sup>

### Powder X-ray diffraction

PXRD data were obtained at room temperature for ground crystalline samples loaded into glass capillaries (0.5 mm in diameter for structural measurements, 0.7 mm for phase purity measurements). Different hydration states presented in the Fig. 1b were stabilized in the following conditions: I and VII – saturated water vapor at 298 K (RH  $\approx$  100%, sample in the capillary was always covered with a drop of distilled water to maintain high humidity conditions during the course of the measurement), II – saturated LiCl solution at 298 K (RH = 11.3 ± 0.3%), III – saturated KOH solution at 313 K (RH = 6.3 ± 0.4%), IV – dry argon atmosphere at 298 K, V – saturated LiCl solution at 298 K (RH = 11.3 ± 0.3%) and VI – saturated CH<sub>3</sub>-COOK solution at 313 K (RH = 18.7 ± 0.5%).<sup>111</sup> Phase purity measurements were subjected to background correction using the DIFFRAC algorithm implemented in the DIFFRAC.EVA V5 software. The measurements were carried out using Bruker D8 Advance diffractometer (Cu K $\alpha$  radiation, graphite monochromator). The unit cell parameters of **1Mn**, **1Mn**·2H<sub>2</sub>O, **1Mn**·3H<sub>2</sub>O were determined using the Winplotr and DICVOL06 indexing software.<sup>116,117</sup> The obtained parameters were refined by fitting the experimental pattern according to the LeBail method in JANA2006.<sup>118</sup> The structure determination was performed using a direct-space method FOX software.<sup>119</sup> The starting models consisted of three molecular fragments: one  $[\text{Mo}^{\text{IV}}(\text{CN})_8]^{4-}$  and two  $[\text{Mn}^{\text{II}}(\text{imH})]^{2+}$  (or  $[\text{Mn}^{\text{II}}(\text{imH})(\text{H}_2\text{O})]^{2+}$  /  $[\text{Mn}^{\text{II}}(\text{imH})(\text{H}_2\text{O})_2]^{2+}$  in the case of **1Mn**·2H<sub>2</sub>O and **1Mn**·3H<sub>2</sub>O) with bond distances and angles based on the single crystal model of **1Mn**·8H<sub>2</sub>O. The obtained preliminary models were, subsequently, refined using the JANA2006 Rietveld software keeping the fragments rigid. The final agreement factors are presented in ESI (Tables S1 and S2†).

### Physical characterization

The dynamic vapor sorption measurements were performed using an SMS DVS Resolution apparatus for an initial sample mass of 5–10 mg. Sample mass at each step of water sorption isotherm was assumed stable after reaching the  $dm/dt < 0.002\% m_0 \text{ min}^{-1}$  limit. The isosteric enthalpy of water adsorption for each point of adsorption isotherm at 298 K was calculated by interpolating data obtained at 313 K to the corresponding data points at 298 K (Table S3†) and then applying the van't Hoff equation:

$$\Delta H_{\text{ads}} = -R \ln \left( \frac{p_2}{p_1} \right) \frac{T_1 T_2}{T_2 - T_1}$$

Average adsorption enthalpy was determined by integrating the obtained curve (Fig. S16†) within  $\Delta m/m_0 = 1.5\text{--}25.4\%$  and then dividing by the range. The QE-TPDA measurements were performed using a homemade thermodesorption apparatus (equipped with a VICI Microvolume TCD-2 thermal conductivity detector, electronic mass flow controllers of the carrier gas Brooks 5850, and a passive room temperature saturator) described in details elsewhere.<sup>100–104</sup> TGA was performed using a NETZSCH TG 209 F1 Libra under a flow of nitrogen (20 mL min<sup>−1</sup>). The DSC measurement was performed with the use



of a Mettler Toledo DSC 822e. After reaching 200 °C the measurement of the heating curve was repeated and the second measurement for the anhydrous sample was used as background. Average water adsorption enthalpy from calorimetric measurement was calculated by integrating the DSC curve and dividing the obtained value by the total number of water molecules. Elemental analyses were performed using an ELEMENTAR Vario Micro Cube CHNS analyzer. SEM measurements were performed using Hitachi S-4700 FE-SEM scanning electron microscope.

### EPR spectroscopy

Continuous-wave EPR spectra in X-band were conducted on a Bruker Elexsys E500 spectrometer (Faculty of Chemistry, Jagiellonian University, Kraków, Poland). *In situ* dehydration-rehydration experiments in X-band were conducted on a Bruker Elexsys E580 spectrometer (Department of Molecular Biophysics, Jagiellonian University, Kraków, Poland). These measurements were performed in a quartz tube shaped like a Pasteur pipette. The narrow side of the tube was closed with a piece of a KIMTECH SCIENCE\* Precision Wipe, on which a small amount (*ca.* 3 mg) of the sample was placed. Tygon® tubing was used to connect the broad side of the quartz tube with an adapter equipped with a glass stopcock, that was used to deliver purge gas to the sample. In the dehydration experiment, it was connected directly to the source of dry nitrogen gas, while in the rehydration experiment – the nitrogen gas was passed through a water bubbler.

### Other spectroscopic measurements

Infrared spectra were recorded using a Nicolet iN10 MX FT-IR microscope in the transmission mode (a small amount of powdered sample was spread on BaF<sub>2</sub> pellet). Dehydration-rehydration experiments were performed with the use of a Linkam THMS350V stage. UV-vis spectra were measured in transmission mode for samples mixed with paraffin oil between two quartz slides using a PerkinElmer Lambda 35 UV/VIS spectrophotometer equipped with an integrating sphere.

### Magnetic and photomagnetic measurements

Magnetic susceptibility measurements were performed using a Quantum Design MPMS-3 Evercool magnetometer in magnetic fields up to 7 T for samples packed into Delrin sample holders.<sup>120</sup> The experimental data were corrected for the diamagnetism of the sample and the sample holder. Photomagnetic measurements were performed for samples placed between two layers of scotch tape and inserted into the plastic straw. **1Mn** was prepared for photomagnetic measurements in the oxygen- and water-free glovebox to prevent its rehydration and **1Mn·8H<sub>2</sub>O** was inserted into the magnetometer and vacuum pumped below 240 K to avoid its dehydration. Irradiation was performed using 450 nm light produced by a laser diode (L450P1600MM; power at the sample position 6–10 mW cm<sup>-2</sup>).

## Data availability

CCDC 2046137 (**1Mn·8H<sub>2</sub>O**), 2046138 (**2Cd·8H<sub>2</sub>O**), 2048781 (**1Mn·3H<sub>2</sub>O**), 2048780 (**1Mn·8H<sub>2</sub>O**) and 2048779 (**1Mn**) contain the supplementary crystallographic data for this paper.

## Author contributions

M. Magott: conceptualization, funding acquisition, investigation (synthesis, X-ray diffraction, TGA, magnetic and photomagnetic measurements, part of EPR and DVS experiments), writing – original draft, writing – review & editing, B. Gaweł: investigation and formal analysis (determination of PXRD structures), M. Sarewicz: investigation and supervision (EPR), M. Reczyński: investigation and supervision (water vapour sorption measurements using DVS), writing – review & editing, K. Ogorzały: investigation (QE-TPDA), W. Makowski: funding acquisition, investigation and supervision (QE-TPDA), D. Pinkowicz: conceptualization, funding acquisition, project administration, supervision (magnetic and photomagnetic measurements), writing – review & editing. All authors reviewed and agreed to the final version of the manuscript.

## Conflicts of interest

There are no conflicts to declare.

## Acknowledgements

This work was financed by the Polish Ministry of Science and Higher Education within the Diamond Grant (0192/DIA/2017/46) and the Polish National Science Centre within the Sonata Bis 6 (2016/22/E/ST5/00055). WM gratefully acknowledges Polish National Science Centre for the financial support of the QE-TPDA characterization within the Opus 15 (2018/29/B/ST4/00328) project. The authors gratefully acknowledge Prof. Artur Osyczka for providing access to the EPR facility of the Faculty of Biochemistry, Biophysics and Biotechnology, Department of Molecular Biophysics.

## References

- 1 H. Furukawa, K. E. Cordova, M. O'Keeffe and O. M. Yaghi, *Science*, 2013, **341**, 1230444.
- 2 O. M. Yaghi, M. J. Kalmutzki and C. S. Diercks, *Introduction to Reticular Chemistry: Metal–Organic Frameworks and Covalent Organic Frameworks*, Wiley-VCH Verlag GmbH & Co. KGaA, 2019.
- 3 O. K. Farha, A. Özgür Yazaydin, I. Eryazici, C. D. Malliakas, B. G. Hauser, M. G. Kanatzidis, S. T. Nguyen, R. Q. Snurr and J. T. Hupp, *Nat. Chem.*, 2010, **2**, 944–948.
- 4 D. Yuan, D. Zhao, D. Sun and H.-C. Zhou, *Angew. Chem., Int. Ed.*, 2010, **49**, 5357–5361.
- 5 H. Furukawa, N. Ko, Y. B. Go, N. Aratani, S. B. Choi, E. Choi, A. Ö. Yazaydin, R. Q. Snurr, M. O'Keeffe, J. Kim and O. M. Yaghi, *Science*, 2010, **329**, 424.



- 6 L. E. Kreno, K. Leong, O. K. Farha, M. Allendorf, R. P. Van Duyne and J. T. Hupp, *Chem. Rev.*, 2012, **112**, 1105–1125.
- 7 J. Zhang, W. Kosaka, Y. Kitagawa and H. Miyasaka, *Nat. Chem.*, 2021, **13**, 191–199.
- 8 J. Canivet, A. Fateeva, Y. Guo, B. Coasne and D. Farrusseng, *Chem. Soc. Rev.*, 2014, **43**, 5594–5617.
- 9 H. Furukawa, F. Gándara, Y.-B. Zhang, J. Jiang, W. L. Queen, M. R. Hudson and O. M. Yaghi, *J. Am. Chem. Soc.*, 2014, **136**, 4369–4381.
- 10 S. Bourrelly, B. Moulin, A. Rivera, G. Maurin, S. Devautour-Vinot, C. Serre, T. Devic, P. Horcajada, A. Vimont, G. Clet, M. Daturi, J.-C. Lavalley, S. Loera-Serna, R. Denoyel, P. L. Llewellyn and G. Férey, *J. Am. Chem. Soc.*, 2010, **132**, 9488–9498.
- 11 Z. Lin, R. Zou, J. Liang, W. Xia, D. Xia, Y. Wang, J. Lin, T. Hu, Q. Chen, X. Wang, Y. Zhao and A. K. Burrell, *J. Mater. Chem.*, 2012, **22**, 7813–7818.
- 12 A. Shigematsu, T. Yamada and H. Kitagawa, *J. Am. Chem. Soc.*, 2012, **134**, 13145–13147.
- 13 Y. Tang, D. Dubbeldam, X. Guo, G. Rothenberg and S. Tanase, *ACS Appl. Mater. Interfaces*, 2019, **11**, 21126–21136.
- 14 K. J. Hartlieb, J. M. Holcroft, P. Z. Moghadam, N. A. Vermeulen, M. M. Algaradah, M. S. Nassar, Y. Y. Botros, R. Q. Snurr and J. F. Stoddart, *J. Am. Chem. Soc.*, 2016, **138**, 2292–2301.
- 15 J. Navarro-Sánchez, A. I. Argente-García, Y. Moliner-Martínez, D. Roca-Sanjuán, D. Antypov, P. Campins-Falcó, M. J. Rosseinsky and C. Martí-Gastaldo, *J. Am. Chem. Soc.*, 2017, **139**, 4294–4297.
- 16 V. Lykourinou, Y. Chen, X.-S. Wang, L. Meng, T. Hoang, L.-J. Ming, R. L. Musselman and S. Ma, *J. Am. Chem. Soc.*, 2011, **133**, 10382–10385.
- 17 H. Deng, S. Grunder, K. E. Cordova, C. Valente, H. Furukawa, M. Hmadeh, F. Gándara, A. C. Whalley, Z. Liu, S. Asahina, H. Kazumori, M. O'Keeffe, O. Terasaki, J. F. Stoddart and O. M. Yaghi, *Science*, 2012, **336**, 1018.
- 18 H. Kim, S. Yang, S. R. Rao, S. Narayanan, E. A. Kapustin, H. Furukawa, A. S. Umans, O. M. Yaghi and E. N. Wang, *Science*, 2017, **356**, 430.
- 19 M. J. Kalmutzki, C. S. Diercks and O. M. Yaghi, *Adv. Mater.*, 2018, **30**, 1704304.
- 20 A. J. Rieth, A. M. Wright, G. Skorupskii, J. L. Mancuso, C. H. Hendon and M. Dincă, *J. Am. Chem. Soc.*, 2019, **141**, 13858–13866.
- 21 N. Hanikel, M. S. Prévot, F. Fathieh, E. A. Kapustin, H. Lyu, H. Wang, N. J. Diercks, T. G. Glover and O. M. Yaghi, *ACS Cent. Sci.*, 2019, **5**, 1699–1706.
- 22 M. W. Logan, S. Langevin and Z. Xia, *Sci. Rep.*, 2020, **10**, 1492.
- 23 A. Khutia, H. U. Rammelberg, T. Schmidt, S. Henninger and C. Janiak, *Chem. Mater.*, 2013, **25**, 790–798.
- 24 M. F. de Lange, K. J. F. M. Verouden, T. J. H. Vlugt, J. Gascon and F. Kapteijn, *Chem. Rev.*, 2015, **115**, 12205–12250.
- 25 A. J. Rieth, A. M. Wright, S. Rao, H. Kim, A. D. LaPotin, E. N. Wang and M. Dincă, *J. Am. Chem. Soc.*, 2018, **140**, 17591–17596.
- 26 A. P. Côté, A. I. Benin, N. W. Ockwig, M. Keffe, A. J. Matzger and O. M. Yaghi, *Science*, 2005, **310**, 1166.
- 27 B. P. Biswal, S. Kandambeth, S. Chandra, D. B. Shinde, S. Bera, S. Karak, B. Garai, U. K. Kharul and R. Banerjee, *J. Mater. Chem. A*, 2015, **3**, 23664–23669.
- 28 S. Jhulki, A. M. Evans, X.-L. Hao, M. W. Cooper, C. H. Feriante, J. Leisen, H. Li, D. Lam, M. C. Hersam, S. Barlow, J.-L. Brédas, W. R. Dichtel and S. R. Marder, *J. Am. Chem. Soc.*, 2020, **142**, 783–791.
- 29 H. L. Nguyen, N. Hanikel, S. J. Lyle, C. Zhu, D. M. Proserpio and O. M. Yaghi, *J. Am. Chem. Soc.*, 2020, **142**, 2218–2221.
- 30 A. J. Howarth, Y. Liu, P. Li, Z. Li, T. C. Wang, J. T. Hupp and O. K. Farha, *Nat. Rev. Mater.*, 2016, **1**, 15018.
- 31 S. S. Kaye and J. R. Long, *J. Am. Chem. Soc.*, 2005, **127**, 6506–6507.
- 32 K. W. Chapman, P. D. Southon, C. L. Weeks and C. J. Kepert, *Chem. Commun.*, 2005, 3322–3324.
- 33 C. P. Krap, J. Balmaseda, L. F. del Castillo, B. Zamora and E. Reguera, *Energy Fuels*, 2010, **24**, 581–589.
- 34 C. P. Krap, J. Balmaseda, B. Zamora and E. Reguera, *Int. J. Hydrogen Energy*, 2010, **35**, 10381–10386.
- 35 A. Takahashi, H. Tanaka, D. Parajuli, T. Nakamura, K. Minami, Y. Sugiyama, Y. Hakuta, S.-i. Ohkoshi and T. Kawamoto, *J. Am. Chem. Soc.*, 2016, **138**, 6376–6379.
- 36 Y. Jiang, A. Takahashi, T. Kawamoto, M. Asai, N. Zhang, Z. Lei, Z. Zhang, K. Kojima, K. Imoto, K. Nakagawa, S.-i. Ohkoshi and T. Nakamura, *Chem. Commun.*, 2018, **54**, 11961–11964.
- 37 Y. Jiang, A. Takahashi, T. Kawamoto, M. Asai, N. Zhang, Z. Lei, Z. Zhang, K. Kojima and T. Nakamura, *Inorg. Chim. Acta*, 2020, **501**, 119273.
- 38 H. Li, M. Eddaoudi, M. O'Keeffe and O. M. Yaghi, *Nature*, 1999, **402**, 276–279.
- 39 N. C. Burtch, I. M. Walton, J. T. Hungerford, C. R. Morelock, Y. Jiao, J. Heinen, Y.-S. Chen, A. A. Yakovenko, W. Xu, D. Dubbeldam and K. S. Walton, *Nat. Chem.*, 2020, **12**, 186–192.
- 40 O. Stefańczyk and S.-i. Ohkoshi, *Chem.-Eur. J.*, 2019, **25**, 15963–15977.
- 41 S. Chorazy, J. J. Zakrzewski, M. Magott, T. Korzeniak, B. Nowicka, D. Pinkowicz, R. Podgajny and B. Sieklucka, *Chem. Soc. Rev.*, 2020, **49**, 5945–6001.
- 42 G. Agustí, R. Ohtani, K. Yoneda, A. B. Gaspar, M. Ohba, J. F. Sánchez-Royo, M. C. Muñoz, S. Kitagawa and J. A. Real, *Angew. Chem., Int. Ed.*, 2009, **48**, 8944–8947.
- 43 P. D. Southon, L. Liu, E. A. Fellows, D. J. Price, G. J. Halder, K. W. Chapman, B. Moubaraki, K. S. Murray, J.-F. Létard and C. J. Kepert, *J. Am. Chem. Soc.*, 2009, **131**, 10998–11009.
- 44 M. Ohba, K. Yoneda, G. Agustí, M. C. Muñoz, A. B. Gaspar, J. A. Real, M. Yamasaki, H. Ando, Y. Nakao, S. Sakaki and S. Kitagawa, *Angew. Chem., Int. Ed.*, 2009, **48**, 4767–4771.
- 45 D. Pinkowicz, R. Podgajny, M. Bałanda, M. Makarewicz, B. Gawel, W. Łasocha and B. Sieklucka, *Inorg. Chem.*, 2008, **47**, 9745–9747.
- 46 D. Pinkowicz, R. Podgajny, B. Gawel, W. Nitek, W. Łasocha, M. Oszejka, M. Czapla, M. Makarewicz, M. Bałanda and B. Sieklucka, *Angew. Chem., Int. Ed.*, 2011, **50**, 3973–3977.



- 47 M. Magott, M. Reczyński, B. Gaweł, B. Sieklucka and D. Pinkowicz, *J. Am. Chem. Soc.*, 2018, **140**, 15876–15882.
- 48 J. Larionova, S. A. Chavan, J. V. Yakhmi, A. G. Frøystein, J. Sletten, C. Sourisseau and O. Kahn, *Inorg. Chem.*, 1997, **36**, 6374–6381.
- 49 O. Kahn, J. Larionova and J. V. Yakhmi, *Chem.–Eur. J.*, 1999, **5**, 3443–3449.
- 50 L. Shen, Y. Zhang and J. Uiu, *J. Coord. Chem.*, 2006, **59**, 629–635.
- 51 C. Serre, F. Millange, C. Thouvenot, M. Noguès, G. Marsolier, D. Louër and G. Férey, *J. Am. Chem. Soc.*, 2002, **124**, 13519–13526.
- 52 C. Mellot-Draznieks, C. Serre, S. Surblé, N. Audebrand and G. Férey, *J. Am. Chem. Soc.*, 2005, **127**, 16273–16278.
- 53 A. Schneemann, V. Bon, I. Schwedler, I. Senkovska, S. Kaskel and R. A. Fischer, *Chem. Soc. Rev.*, 2014, **43**, 6062–6096.
- 54 E. Coronado, M. Giménez-Marqués, G. M. Espallargas and L. Brammer, *Nat. Commun.*, 2012, **3**, 828.
- 55 I.-R. Jeon, B. Negru, R. P. Van Duyne and T. D. Harris, *J. Am. Chem. Soc.*, 2015, **137**, 15699–15702.
- 56 W. Kosaka, Z. Liu, J. Zhang, Y. Sato, A. Hori, R. Matsuda, S. Kitagawa and H. Miyasaka, *Nat. Commun.*, 2018, **9**, 5420.
- 57 L. Liu, J. A. DeGayner, L. Sun, D. Z. Zee and T. D. Harris, *Chem. Sci.*, 2019, **10**, 4652–4661.
- 58 L. Qu, H. Iguchi, S. Takaishi, F. Habib, C. F. Leong, D. M. D'Alessandro, T. Yoshida, H. Abe, E. Nishibori and M. Yamashita, *J. Am. Chem. Soc.*, 2019, **141**, 6802–6806.
- 59 J. Chen, Y. Sekine, A. Okazawa, H. Sato, W. Kosaka and H. Miyasaka, *Chem. Sci.*, 2020, **11**, 3610–3618.
- 60 A. E. Thorarinsdottir and T. D. Harris, *Chem. Rev.*, 2020, **120**, 8716–8789.
- 61 A. M. Sheveleva, D. I. Kolokolov, A. A. Gabrienko, A. G. Stepanov, S. A. Gromilov, I. K. Shundrina, R. Z. Sagdeev, M. V. Fedin and E. G. Bagryanskaya, *J. Phys. Chem. Lett.*, 2014, **5**, 20–24.
- 62 M. Mendt, F. Gutt, N. Kavoosi, V. Bon, I. Senkovska, S. Kaskel and A. Pöppel, *J. Phys. Chem. C*, 2016, **120**, 14246–14259.
- 63 A. T. Gallagher, C. D. Malliakas and T. D. Harris, *Inorg. Chem.*, 2017, **56**, 4654–4661.
- 64 X. Han, H. G. W. Godfrey, L. Briggs, A. J. Davies, Y. Cheng, L. L. Daemen, A. M. Sheveleva, F. Tuna, E. J. L. McInnes, J. Sun, C. Drathen, M. W. George, A. J. Ramirez-Cuesta, K. M. Thomas, S. Yang and M. Schröder, *Nat. Mater.*, 2018, **17**, 691–696.
- 65 J. Li, X. Han, X. Zhang, A. M. Sheveleva, Y. Cheng, F. Tuna, E. J. L. McInnes, L. J. McCormick McPherson, S. J. Teat, L. L. Daemen, A. J. Ramirez-Cuesta, M. Schröder and S. Yang, *Nat. Chem.*, 2019, **11**, 1085–1090.
- 66 Y. Jiang, J. Huang, B. Kasumaj, G. Jeschke, M. Hunger, T. Mallat and A. Baiker, *J. Am. Chem. Soc.*, 2009, **131**, 2058–2059.
- 67 A. Kultaeva, V. Bon, M. S. Weiss, A. Pöppel and S. Kaskel, *Inorg. Chem.*, 2018, **57**, 11920–11929.
- 68 A. S. Poryvaev, A. M. Sheveleva, P. A. Demakov, S. S. Arzumanov, A. G. Stepanov, D. N. Dybtsev and M. V. Fedin, *Appl. Magn. Reson.*, 2018, **49**, 255–264.
- 69 M. Hunger and J. Weitkamp, *Angew. Chem., Int. Ed.*, 2001, **40**, 2954–2971.
- 70 A. Brückner, *Chem. Soc. Rev.*, 2010, **39**, 4673–4684.
- 71 K. Sobańska, P. Pietrzyk and Z. Sojka, *ACS Catal.*, 2017, **7**, 2935–2947.
- 72 P. Pietrzyk, K. Góra-Marek, T. Mazur, B. Mozgawa, M. Radoń, M. Chiesa, Z. Zhao and Z. Sojka, *J. Catal.*, 2021, **394**, 206–219.
- 73 H. Reinsch, M. A. van der Veen, B. Gil, B. Marszalek, T. Verbiest, D. de Vos and N. Stock, *Chem. Mater.*, 2013, **25**, 17–26.
- 74 G. Wißmann, A. Schaate, S. Lilienthal, I. Bremer, A. M. Schneider and P. Behrens, *Microporous Mesoporous Mater.*, 2012, **152**, 64–70.
- 75 J. H. Cavka, S. Jakobsen, U. Olsbye, N. Guillou, C. Lamberti, S. Bordiga and K. P. Lillerud, *J. Am. Chem. Soc.*, 2008, **130**, 13850–13851.
- 76 N. L. Rosi, J. Kim, M. Eddaoudi, B. L. Chen, M. O'Keeffe and O. M. Yaghi, *J. Am. Chem. Soc.*, 2005, **127**, 1504–1518.
- 77 A. J. Rieth, S. Yang, E. N. Wang and M. Dincă, *ACS Cent. Sci.*, 2017, **3**, 668–672.
- 78 G. Férey, C. Mellot-Draznieks, C. Serre, F. Millange, J. Dutour, S. Surblé and I. Margiolaki, *Science*, 2005, **309**, 2040.
- 79 P. Küsgens, M. Rose, I. Senkovska, H. Fröde, A. Henschel, S. Siegle and S. Kaskel, *Microporous Mesoporous Mater.*, 2009, **120**, 325–330.
- 80 K. Roztocki, F. Formalik, A. Krawczuk, I. Senkovska, B. Kuchta, S. Kaskel and D. Matoga, *Angew. Chem., Int. Ed.*, 2020, **59**, 4491–4497.
- 81 T. Loiseau, C. Serre, C. Huguenard, G. Fink, F. Taulelle, M. Henry, T. Bataille and G. Férey, *Chem.–Eur. J.*, 2004, **10**, 1373–1382.
- 82 J. Canivet, J. Bonnefoy, C. Daniel, A. Legrand, B. Coasne and D. Farrusseng, *New J. Chem.*, 2014, **38**, 3102–3111.
- 83 B.-Q. Song, Q.-Y. Yang, S.-Q. Wang, M. Vandichel, A. Kumar, C. Crowley, N. Kumar, C.-H. Deng, V. GasconPerez, M. Lusi, H. Wu, W. Zhou and M. J. Zaworotko, *J. Am. Chem. Soc.*, 2020, **142**, 6896–6901.
- 84 Q.-L. Wang, H. Southerland, J.-R. Li, A. V. Prosvirin, H. Zhao and K. R. Dunbar, *Angew. Chem., Int. Ed.*, 2012, **51**, 9321–9324.
- 85 S. Tanase, F. Tuna, P. Guionneau, T. Maris, G. Rombaut, C. Mathonière, M. Andruh, O. Kahn and J.-P. Sutter, *Inorg. Chem.*, 2003, **42**, 1625–1631.
- 86 S.-i. Ohkoshi, Y. Tsunobuchi, H. Takahashi, T. Hozumi, M. Shiro and K. Hashimoto, *J. Am. Chem. Soc.*, 2007, **129**, 3084–3085.
- 87 T. Yoshihide, H. Kazuhito, S. Motoo, H. Toshiya and O. Shin-ichi, *Chem. Lett.*, 2007, **36**, 1464–1465.
- 88 M. Reczyński, S. Chorazy, B. Nowicka, B. Sieklucka and S.-i. Ohkoshi, *Inorg. Chem.*, 2017, **56**, 179–185.





- 89 K. Imoto, D. Takahashi, Y. Tsunobuchi, W. Kosaka, M. Arai, H. Tokoro and S.-i. Ohkoshi, *Eur. J. Inorg. Chem.*, 2010, **2010**, 4079–4082.
- 90 K. Komori-Orisaku, O. Stefańczyk, S. Ohishi, N. Ozaki, Y. Miyamoto, K. Imoto and S.-i. Ohkoshi, *Chem.–Eur. J.*, 2019, **25**, 11066–11073.
- 91 B. Nowicka, M. Rams, K. Stadnicka and B. Sieklucka, *Inorg. Chem.*, 2007, **46**, 8123–8125.
- 92 B. Nowicka, M. Balańda, B. Gawęł, G. Ćwiak, A. Budziak, W. Łasocha and B. Sieklucka, *Dalton Trans.*, 2011, **40**, 3067–3073.
- 93 H. Chun, D. N. Dybtsev, H. Kim and K. Kim, *Chem.–Eur. J.*, 2005, **11**, 3521–3529.
- 94 B. Bueken, H. Reinsch, N. Reimer, I. Stassen, F. Vermoortele, R. Ameloot, N. Stock, C. E. A. Kirschhock and D. De Vos, *Chem. Commun.*, 2014, **50**, 10055–10058.
- 95 F.-X. Coudert, A. U. Ortiz, V. Haigis, D. Bousquet, A. H. Fuchs, A. Ballandras, G. Weber, I. Bezverkhyy, N. Geoffroy, J.-P. Bellat, G. Ortiz, G. Chaplais, J. Patarin and A. Boutin, *J. Phys. Chem. C*, 2014, **118**, 5397–5405.
- 96 S. Devautour-Vinot, G. Maurin, F. Henn, C. Serre and G. Férey, *Phys. Chem. Chem. Phys.*, 2010, **12**, 12478–12485.
- 97 M. J. Kalmutzki, N. Hanikel and O. M. Yaghi, *Sci. Adv.*, 2018, **4**, eaat9180.
- 98 S. Vyazovkin, A. K. Burnham, J. M. Criado, L. A. Pérez-Maqueda, C. Popescu and N. Sbirrazzuoli, *Thermochim. Acta*, 2011, **520**, 1–19.
- 99 R. L. Blaine and H. E. Kissinger, *Thermochim. Acta*, 2012, **540**, 1–6.
- 100 W. Makowski, *Thermochim. Acta*, 2007, **454**, 26–32.
- 101 W. Makowski, B. Gil and D. Majda, *Catal. Lett.*, 2008, **120**, 154–160.
- 102 M. Mańko, B. Gil, R. Janus, P. Kuśtrowski and W. Makowski, *Thermochim. Acta*, 2010, **511**, 82–88.
- 103 K. Roztocki, M. Lupa, A. Sławek, W. Makowski, I. Senkovska, S. Kaskel and D. Matoga, *Inorg. Chem.*, 2018, **57**, 3287–3296.
- 104 A. Sławek, J. M. Vicent-Luna, B. Marszałek, B. Gil, R. E. Morris, W. Makowski and S. Calero, *Chem. Mater.*, 2018, **30**, 5116–5127.
- 105 R. Jankowski, M. Reczyński, S. Chorazy, M. Zychowicz, M. Arczyński, M. Koziół, K. Ogorzały, W. Makowski, D. Pinkowicz and B. Sieklucka, *Chem.–Eur. J.*, 2020, **26**, 11187–11198.
- 106 S. Stoll and A. Schweiger, *J. Magn. Reson.*, 2006, **178**, 42–55.
- 107 N. Bridonneau, J. Long, J. L. Cantin, J. von Bardeleben, S. Pillet, E. E. Bendeif, D. Aravena, E. Ruiz and V. Marvaud, *Chem. Commun.*, 2015, **51**, 8229–8232.
- 108 M. Magott, O. Stefańczyk, B. Sieklucka and D. Pinkowicz, *Angew. Chem., Int. Ed.*, 2017, **56**, 13283–13287.
- 109 X. Qi, S. Pillet, C. de Graaf, M. Magott, E.-E. Bendeif, P. Guionneau, M. Rouzières, V. Marvaud, O. Stefańczyk, D. Pinkowicz and C. Mathonière, *Angew. Chem., Int. Ed.*, 2020, **59**, 3117–3121.
- 110 G. Handzlik, M. Magott, B. Sieklucka and D. Pinkowicz, *Eur. J. Inorg. Chem.*, 2016, **2016**, 4872–4877.
- 111 L. Greenspan, *J. Res. Natl. Bur. Stand., Sect. A*, 1977, **81**, 89–96.
- 112 G. Sheldrick, *Acta Crystallogr., Sect. A: Found. Crystallogr.*, 2008, **64**, 112–122.
- 113 O. V. Dolomanov, L. J. Bourhis, R. J. Gildea, J. A. K. Howard and H. Puschmann, *J. Appl. Crystallogr.*, 2009, **42**, 339–341.
- 114 G. Sheldrick, *Acta Crystallogr., Sect. C: Struct. Chem.*, 2015, **71**, 3–8.
- 115 C. F. Macrae, I. Sovago, S. J. Cottrell, P. T. A. Galek, P. McCabe, E. Pidcock, M. Platings, G. P. Shields, J. S. Stevens, M. Towler and P. A. Wood, *J. Appl. Crystallogr.*, 2020, **53**, 226–235.
- 116 T. Roisnel and J. Rodríguez-Carvajal, *Mater. Sci. Forum*, 2001, **378–381**, 118–123.
- 117 A. Boultif and D. Louer, *J. Appl. Crystallogr.*, 2004, **37**, 724–731.
- 118 V. Petříček, M. Dušek and L. Palatinus, *Z. Kristallogr. - Cryst. Mater.*, 2014, **229**, 345–352.
- 119 V. Favre-Nicolin and R. Cerny, *J. Appl. Crystallogr.*, 2002, **35**, 734–743.
- 120 M. Arczyński, J. Stanek, B. Sieklucka, K. R. Dunbar and D. Pinkowicz, *J. Am. Chem. Soc.*, 2019, **141**, 19067–19077.

